^{4}He microscopic optical model potential

Hairui Guo,[1,*] Yongli Xu,[1,2] Haiying Liang,[1] Yinlu Han,[1,†] and Qingbiao Shen[1]
[1]*China Institute of Atomic Energy, P.O. Box 275(41), Beijing 102413, People's Republic of China*
[2]*College of Physics and Electronic Science, Shanxi Datong University, Datong 037009, People's Republic of China*
(Received 15 November 2010; revised manuscript received 3 June 2011; published 28 June 2011)

The ^{4}He microscopic optical model potential is obtained by Green's function method through nuclear matter approximation and local density approximation based on the effective Skyrme interaction. The microscopic optical model potential is analyzed and utilized to calculate the reaction cross sections and elastic scattering angular distributions for the target nuclei in the mass range $12 \leqslant A \leqslant 209$ with incident ^{4}He energy up to 400 MeV. The theoretical results are compared with the experimental data.

DOI: 10.1103/PhysRevC.83.064618 PACS number(s): 24.10.Ht, 21.30.Fe, 24.10.Cn, 25.55.−e

I. INTRODUCTION

The study of the microscopic optical model potential (MOP) is one of the most fundamental subjects in the nuclear reaction theory. As the MOP is generated theoretically based on the nucleon-nucleon (N-N) interaction and does not need to adjust parameters to fit the available experimental data like the phenomenological optical model potential does, it has great significance in many branches of nuclear reaction physics, especially in the study of the colliding systems for which the elastic scattering measurement is absent or difficult, such as in the case of neutron-rich or proton-rich β-unstable nuclei.

The ^{4}He MOP is a tool for the understanding of ^{4}He elastic scattering and calculations of α-induced reaction cross sections as well as the α-particle emission from compound reactions. It is of great value for estimating the radiation-damage effect in accelerator-driven system (ADS) and in the research of nuclear astrophysics. The double-folding model (DFM) [1] is generally utilized in the studies of ^{4}He MOP. In the DFM, the optical model potential is generated by doubly folding an effective N-N interaction with the mass distributions of both the target nucleus and the projectile. At present, there are some ^{4}He optical model potentials [2–4] whose real parts are constructed by doubly folding the M3Y N-N interaction or its density- or energy-dependent versions [5–7]. However, the imaginary parts of these potentials are obtained in the phenomenological way. Furumoto *et al.* [8] and Zou *et al.* [9] provide two double-folding potentials of ^{4}He for ^{12}C, ^{16}O, ^{28}Si, and ^{40}Ca, and the real and the imaginary parts of both potentials are obtained in the DFM approach. Furumoto *et al.* adopt the so-called JLM interaction as the complex N-N interaction, and Zou *et al.* use the Dirac-Brueckner-Hartree-Fock G-matrix interaction as the N-N interaction. However, two renormalization parameters are introduced in each double-folding potential to modify the real and imaginary potential strength, respectively, and both the double-folding potentials are finally obtained by adjusting the renormalization parameters to fit the available experimental data. The renormalization parameters vary with different energy and different target nucleus. The renormalization parameters of Furumoto *et al.* modify the real and imaginary potential strength by 22% to 55%, and the parameters of Zou *et al.* modify the real and imaginary potential strength by 24% to 95%.

In the present paper, the ^{4}He MOP is obtained in a different approach. The MOPs of nucleon, deuteron, and ^{3}He are obtained by the Green's function method [10–12]. As the nucleon optical potential is identified with the mass operator of the one-particle Green's function [13], the nucleon microscopic optical potential is obtained by calculating the mass operator through nuclear matter approximation and local density approximation based on some Skyrme interactions [10]. The MOPs of deuteron and ^{3}He are also obtained from the mass operator of the Green's function [11,12]. It is shown that the theoretical results calculated by the MOPs of nucleon, deuteron, and ^{3}He can successfully reproduce the experimental data. Encouraged by the success, the Green's function method is utilized to obtain the ^{4}He MOP in this paper. By this method, the ^{4}He MOP is obtained from the four-particle Green's function based on a Skyrme interaction, and the nuclear matter approximation and local density approximation are also used. The first-order mass operator of the four-particle Green's function denotes the real part of the ^{4}He MOP, and the imaginary part of second-order mass operator denotes the imaginary part of the ^{4}He MOP. The ^{4}He MOP obtained is used to calculate the reaction cross sections and the elastic scattering angular distributions for the target nuclei in the mass range $12 \leqslant A \leqslant 209$ with incident ^{4}He energy up to 400 MeV, and the results are compared with experimental data.

In Sec. II, the formulation of the ^{4}He MOP is presented. Section III is the comparison and analysis of the calculated results and experimental data. Finally, Sec. IV gives a summary.

II. THEORETICAL MODEL

The Hamiltonian of the system composed of the target nucleus and the projectile, which only refers to the two-body

*ghr@ciae.ac.cn
†hanyl@ciae.ac.cn

interaction, can be expressed as

$$H = H_0 + H_1, \tag{1}$$

where

$$H_0 = \sum_i (t_i + U_i), \tag{2}$$

$$H_1 = \frac{1}{2}\sum_{i\neq j} V_{ij} - \sum_i U_i, \tag{3}$$

where t_i is the single-particle kinetic energy operator, U_i is the single-particle mean field, and H_1 is the residual interaction.

The four-particle Green's function is expressed as

$$\begin{aligned} iG(\alpha_1\alpha_2\alpha_3\alpha_4, \beta_1\beta_2\beta_3\beta_4; t_1 - t_2) &= \frac{\langle\phi_0|\, T\left[U_\eta(\infty,-\infty)\xi_{\alpha_4}(t_1)\xi_{\alpha_3}(t_1)\xi_{\alpha_2}(t_1)\xi_{\alpha_1}(t_1)\xi^+_{\beta_1}(t_2)\xi^+_{\beta_2}(t_2)\xi^+_{\beta_3}(t_2)\xi^+_{\beta_4}(t_2)\right]|\phi_0\rangle}{\langle\phi_0|\, U_\eta(\infty,-\infty)\,|\phi_0\rangle} \\ &= \langle\phi_0|\, T\left[U_\eta(\infty,-\infty)\xi_{\alpha_4}(t_1)\xi_{\alpha_3}(t_1)\xi_{\alpha_2}(t_1)\xi_{\alpha_1}(t_1)\xi^+_{\beta_1}(t_2)\xi^+_{\beta_2}(t_2)\xi^+_{\beta_3}(t_2)\xi^+_{\beta_4}(t_2)\right]|\phi_0\rangle_L\,, \end{aligned} \tag{4}$$

where $|\phi_0\rangle$ is the eigenstate of H_0; T is the time-ordering symbol; ξ_{α_1}, ξ_{α_2}, ξ_{α_3}, and ξ_{α_4} are the particle annihilation operators in interaction representation; $\xi^+_{\beta_1}$, $\xi^+_{\beta_2}$, $\xi^+_{\beta_3}$, and $\xi^+_{\beta_4}$ are the particle creation operators; and L denotes that only the linked diagrams are reserved. $U_\eta(\infty,-\infty)$ is the time-evolution operator expressed as

$$U_\eta(\infty,-\infty) = \sum_{n=0}^{\infty}\left(\frac{-i}{\hbar}\right)^n \frac{1}{n!}\int d\tau_1 \int d\tau_2 \cdots \int d\tau_n \exp\left[-\eta(|\tau_1| + |\tau_2| + \cdots + |\tau_n|)\right] T\left\{H_1(\tau_1)H_1(\tau_2)\cdots H_1(\tau_n)\right\}, \tag{5}$$

where η is the infinitesimal introduced from adiabatic approximation.

The four-particle Green's function satisfies the Dyson equation [14–17]:

$$\begin{aligned} iG(\alpha_1\alpha_2\alpha_3\alpha_4, \beta_1\beta_2\beta_3\beta_4;\omega) &= iG^{(0)}(\alpha_1\alpha_2\alpha_3\alpha_4, \beta_1\beta_2\beta_3\beta_4;\omega) + \frac{i}{\hbar}\sum_{\rho\lambda\theta\varepsilon\mu\nu\delta\gamma} iG^{(0)}(\alpha_1\alpha_2\alpha_3\alpha_4, \rho\lambda\theta\varepsilon;\omega)[U_{\rho\lambda\theta\varepsilon,\mu\nu\delta\gamma} \\ &\quad - M(\rho\lambda\theta\varepsilon, \mu\nu\delta\gamma;\omega)]iG(\mu\nu\delta\gamma, \beta_1\beta_2\beta_3\beta_4;\omega), \end{aligned} \tag{6}$$

where

$$G^{(0)}(\alpha_1\alpha_2\alpha_3\alpha_4, \beta_1\beta_2\beta_3\beta_4;\omega) = \delta_{\alpha_1\beta_1}\delta_{\alpha_2\beta_2}\delta_{\alpha_3\beta_3}\delta_{\alpha_4\beta_4}\hbar\left[\frac{(1-n_{\alpha_1})(1-n_{\alpha_2})(1-n_{\alpha_3})(1-n_{\alpha_4})}{\omega-\varepsilon_{\alpha_1}-\varepsilon_{\alpha_2}-\varepsilon_{\alpha_3}-\varepsilon_{\alpha_4}+i\eta} - \frac{n_{\alpha_1}n_{\alpha_2}n_{\alpha_3}n_{\alpha_4}}{\omega-\varepsilon_{\alpha_1}-\varepsilon_{\alpha_2}-\varepsilon_{\alpha_3}-\varepsilon_{\alpha_4}-i\eta}\right], \tag{7}$$

$$n_\alpha = \begin{cases} 1, & \text{below the Fermi surface,} \\ 0, & \text{above the Fermi surface,} \end{cases} \tag{8}$$

$U_{\rho\lambda\theta\varepsilon,\mu\nu\delta\gamma}$ is the mean field, and $M(\rho\lambda\theta\varepsilon, \mu\nu\delta\gamma;\omega)$ is the mass operator which can be expanded into

$$M(\rho\lambda\theta\varepsilon, \mu\nu\delta\gamma;\omega) = M^{(1)}(\rho\lambda\theta\varepsilon, \mu\nu\delta\gamma;\omega) + M^{(2)}(\rho\lambda\theta\varepsilon, \mu\nu\delta\gamma;\omega) + \cdots. \tag{9}$$

For the scattering process, the mass operator $M(\alpha_1\alpha_2\alpha_3\alpha_4, \alpha_1\alpha_2\alpha_3\alpha_4;\omega)$ of the four-particle Green's function is identified with the MOP for ^{4}He.The Eq. (4) can be expanded into perturbation series:

$$\begin{aligned} iG(\alpha_1\alpha_2\alpha_3\alpha_4, \beta_1\beta_2\beta_3\beta_4; t_1 - t_2) &= iG^{(0)}(\alpha_1\alpha_2\alpha_3\alpha_4, \beta_1\beta_2\beta_3\beta_4; t_1 - t_2) + iG^{(1)}(\alpha_1\alpha_2\alpha_3\alpha_4, \beta_1\beta_2\beta_3\beta_4; t_1 - t_2) \\ &\quad + iG^{(2)}(\alpha_1\alpha_2\alpha_3\alpha_4, \beta_1\beta_2\beta_3\beta_4; t_1 - t_2) + \cdots. \end{aligned} \tag{10}$$

It is considered only up to the second order in this paper so as to get the first- and second-order mass operators. The corresponding Feynman diagrams include one zeroth-order diagram, 14 first-order diagrams given in Fig. 1, and 222 second-order diagrams.

When studying the ^{4}He MOP, ^{4}He is considered as a cluster and the nucleon-nucleon direct interaction in ^{4}He is not considered. Because the Feynman diagram in Fig. 1(b) describes the direct interaction of the nucleons in ^{4}He, only the Feynman diagrams in Fig. 1(a) contribute to the first-order term of the four-particle Green's function. By performing the Fourier transformation, the first-order term of the four-particle Green's function can be expressed as

$$\begin{aligned} iG^{(1)}(\alpha_1\alpha_2\alpha_3\alpha_4, \beta_1\beta_2\beta_3\beta_4;\omega) &= \frac{i}{\hbar}iG^{(0)}_{\alpha_1\alpha_2\alpha_3\alpha_4}(\omega)\left[U_{\alpha_1\beta_1} - \sum_\rho V_{\alpha_1\rho,\beta_1\rho}n_\rho\right]iG^{(0)}_{\beta_1\alpha_2\alpha_3\alpha_4}(\omega)\delta_{\alpha_2\beta_2}\delta_{\alpha_3\beta_3}\delta_{\alpha_4\beta_4} + \frac{i}{\hbar}\delta_{\alpha_1\beta_1}iG^{(0)}_{\alpha_1\alpha_2\alpha_3\alpha_4}(\omega) \\ &\quad \cdot\left[U_{\alpha_2\beta_2} - \sum_\rho V_{\alpha_2\rho,\beta_2\rho}n_\rho\right]iG^{(0)}_{\alpha_1\beta_2\alpha_3\alpha_4}(\omega)\delta_{\alpha_3\beta_3}\delta_{\alpha_4\beta_4} + \frac{i}{\hbar}\delta_{\alpha_1\beta_1}\delta_{\alpha_2\beta_2}iG^{(0)}_{\alpha_1\alpha_2\alpha_3\alpha_4}(\omega) \end{aligned}$$

$$\cdot \left[U_{\alpha_3\beta_3} - \sum_\rho V_{\alpha_3\rho,\beta_3\rho} n_\rho \right] i G^{(0)}_{\alpha_1\alpha_2\beta_3\alpha_4}(\omega)\delta_{\alpha_4\beta_4} + \frac{i}{\hbar}\delta_{\alpha_1\beta_1}\delta_{\alpha_2\beta_2}\delta_{\alpha_3\beta_3} i G^{(0)}_{\alpha_1\alpha_2\alpha_3\alpha_4}(\omega)$$
$$\cdot \left[U_{\alpha_4\beta_4} - \sum_\rho V_{\alpha_4\rho,\beta_4\rho} n_\rho \right] i G^{(0)}_{\alpha_1\alpha_2\alpha_3\beta_4}(\omega), \tag{11}$$

where

$$V_{\alpha\rho,\beta\rho} = \langle \alpha\rho |\, V \,| \beta\rho \rangle_A = \langle \alpha\rho |\, V \,| \beta\rho \rangle - \langle \alpha\rho |\, V \,| \rho\beta \rangle\,. \tag{12}$$

A denotes antisymmetrization and V is the two-body nucleon-nucleon interaction.

Equation (11) must satisfy the first-order term of the Dyson equation, which is expressed as

$$\begin{aligned} & i G^{(1)}(\alpha_1\alpha_2\alpha_3\alpha_4,\, \beta_1\beta_2\beta_3\beta_4; \omega) \\ &= \frac{i}{\hbar} i G^{(0)}_{\alpha_1\alpha_2\alpha_3\alpha_4}(\omega)\big[U_{\alpha_1\alpha_2\alpha_3\alpha_4,\beta_1\beta_2\beta_3\beta_4} \\ &\quad - M^{(1)}(\alpha_1\alpha_2\alpha_3\alpha_4,\, \beta_1\beta_2\beta_3\beta_4; \omega)\big] i G^{(0)}_{\beta_1\beta_2\beta_3\beta_4}(\omega). \end{aligned} \tag{13}$$

Under the mean-field approximation,

$$U_{\alpha_1\alpha_2\alpha_3\alpha_4} = U_{\alpha_1} + U_{\alpha_2} + U_{\alpha_3} + U_{\alpha_4} = M^{(1)}_{\alpha_1\alpha_2\alpha_3\alpha_4}, \tag{14}$$

so $M^{(1)}_{\alpha_1\alpha_2\alpha_3\alpha_4}$ gives the real part of the ^{4}He MOP. By comparing Eqs. (11) and (13), the real part of the ^{4}He MOP can be obtained:

$$\begin{aligned} M^{(1)}_{\alpha_1\alpha_2\alpha_3\alpha_4} &= \sum_\rho V_{\alpha_1\rho,\alpha_1\rho} n_\rho + \sum_\rho V_{\alpha_2\rho,\alpha_2\rho} n_\rho \\ &\quad + \sum_\rho V_{\alpha_3\rho,\alpha_3\rho} n_\rho + \sum_\rho V_{\alpha_4\rho,\alpha_4\rho} n_\rho. \end{aligned} \tag{15}$$

In the right-hand side of Eq. (15), each term is just the contribution of the real part of the microscopic optical potential for each nucleon [10] in ^{4}He.

Under the mean-field approximation, 176 of the second-order Feynman diagrams are offset. Figure 2 gives the residual

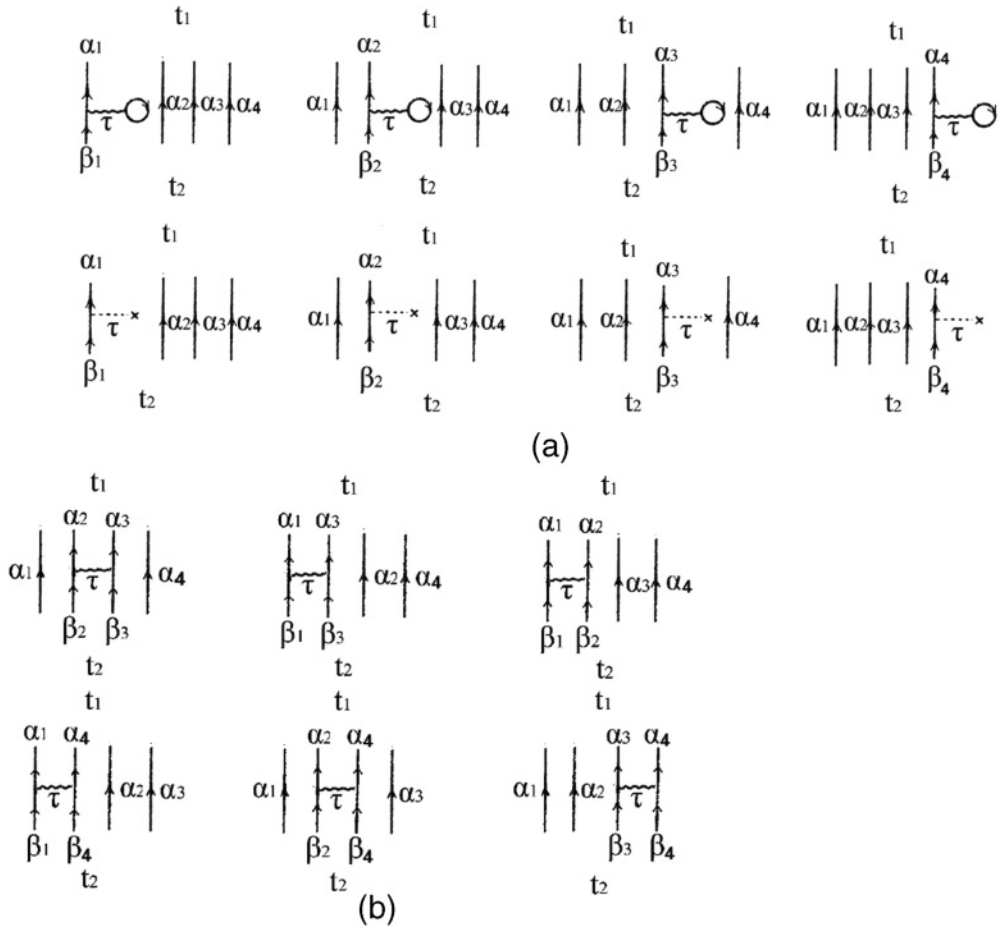

FIG. 1. First-order Feynman diagrams of the four-particle Green's function.

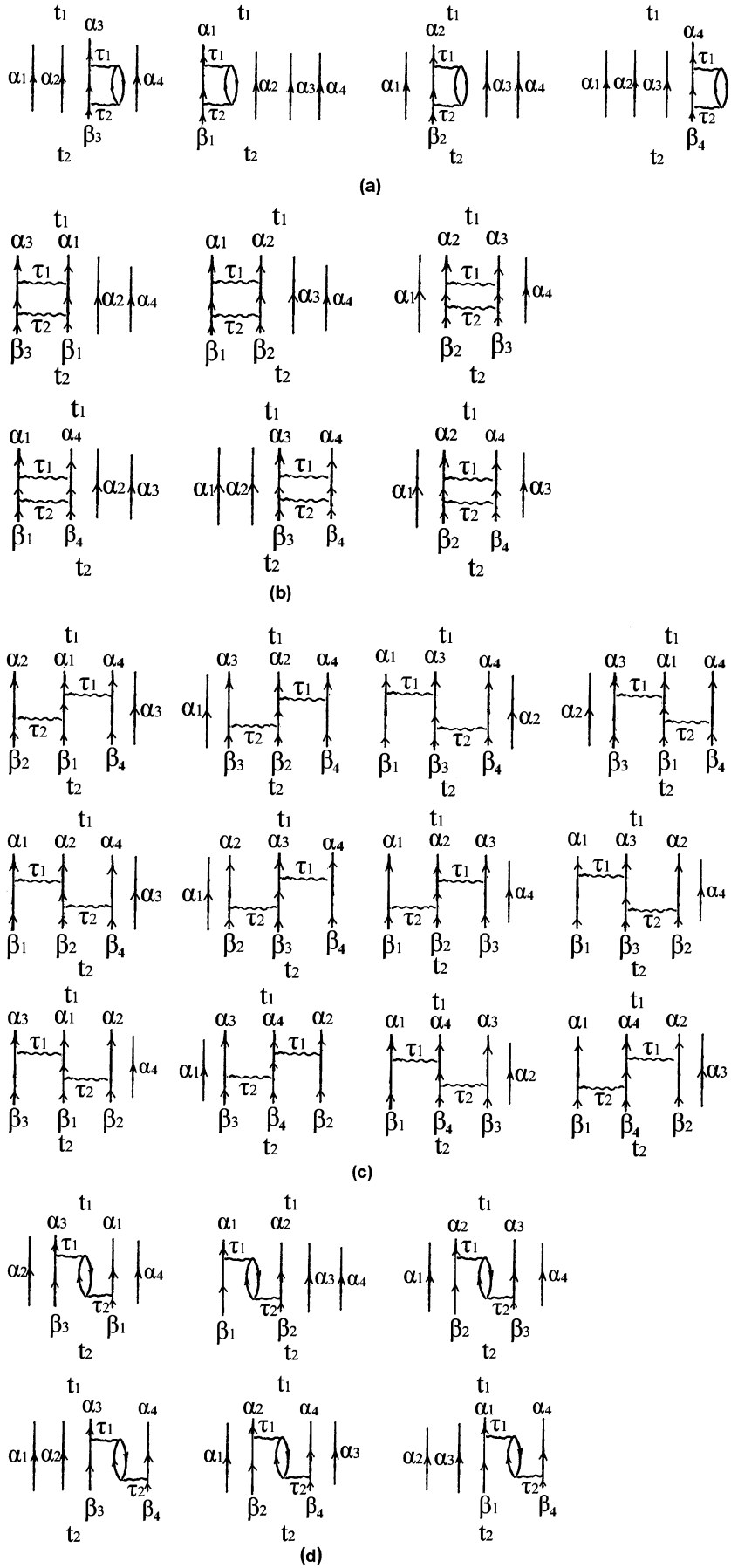

FIG. 2. The residual second-order diagrams of the four-particle Green's function.

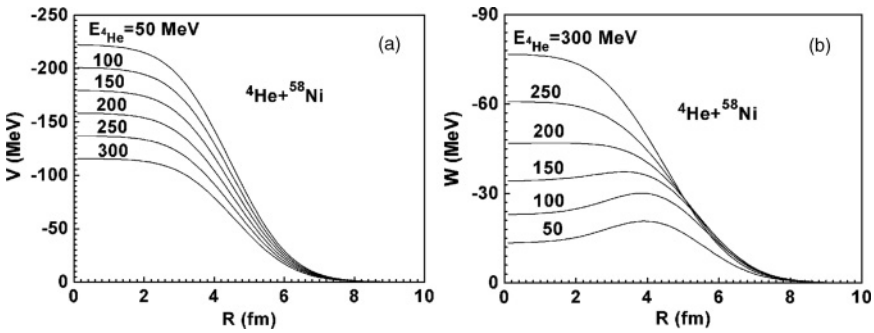

FIG. 3. Radial dependence of ^{4}He MOP for ^{58}Ni. (a) The real parts. (b) The imaginary parts.

second-order Feynman diagrams. The Feynman diagrams in Figs. 2(b) and 2(c) describe the direct interactions of the nucleons in ^{4}He. In Fig. 2(c), when the τ_1 and τ_2, which denote the time when the interactions occur, interchange with each other, another 12 Feynman diagrams describing the direct interactions of the nucleons in ^{4}He will be given. All of these Feynman diagrams describing the direct interactions of the nucleons in ^{4}He can be ignored. The Feynman diagrams in Fig. 2(d) describe the indirect interactions of the nucleons in ^{4}He, which can make ^{4}He break up. The Feynman diagrams in Fig. 2(d) are also ignored. Then only the Feynman diagrams in Fig. 2(a) contribute to the second-order term of the four-particle Green's function.

By performing Fourier transformation, the second-order term of the four-particle Green's function can be expressed as

$$
\begin{aligned}
&iG^{(2)}(\alpha_1\alpha_2\alpha_3\alpha_4,\,\beta_1\beta_2\beta_3\beta_4;\omega)\\
&= -iG^{(0)}_{\alpha_1\alpha_2\alpha_3\alpha_4}(\omega)\frac{i}{\hbar}\left[\frac{1}{2}\sum_{\rho\delta\lambda}\frac{V_{\alpha_2\lambda,\delta\rho}V_{\delta\rho,\beta_2\lambda}}{\omega-\varepsilon_{\alpha_1}-\varepsilon_{\alpha_3}-\varepsilon_{\alpha_4}-\varepsilon_\rho-\varepsilon_\delta+\varepsilon_\lambda+i\eta}n_\lambda(1-n_\delta)(1-n_\rho)\right]iG^{(0)}_{\alpha_1\beta_2\alpha_3\alpha_4}(\omega)\delta_{\alpha_1\beta_1}\delta_{\alpha_3\beta_3}\delta_{\alpha_4\beta_4}\\
&\quad -iG^{(0)}_{\alpha_1\alpha_2\alpha_3\alpha_4}(\omega)\frac{i}{\hbar}\left[\frac{1}{2}\sum_{\rho\delta\lambda}\frac{V_{\alpha_1\lambda,\delta\rho}V_{\delta\rho,\beta_1\lambda}}{\omega-\varepsilon_{\alpha_2}-\varepsilon_{\alpha_3}-\varepsilon_{\alpha_4}-\varepsilon_\rho-\varepsilon_\delta+\varepsilon_\lambda+i\eta}n_\lambda(1-n_\delta)(1-n_\rho)\right]iG^{(0)}_{\beta_1\alpha_2\alpha_3\alpha_4}(\omega)\delta_{\alpha_2\beta_2}\delta_{\alpha_3\beta_3}\delta_{\alpha_4\beta_4}\\
&\quad -iG^{(0)}_{\alpha_1\alpha_2\alpha_3\alpha_4}(\omega)\frac{i}{\hbar}\left[\frac{1}{2}\sum_{\rho\delta\lambda}\frac{V_{\alpha_3\lambda,\delta\rho}V_{\delta\rho,\beta_3\lambda}}{\omega-\varepsilon_{\alpha_1}-\varepsilon_{\alpha_2}-\varepsilon_{\alpha_4}-\varepsilon_\rho-\varepsilon_\delta+\varepsilon_\lambda+i\eta}n_\lambda(1-n_\delta)(1-n_\rho)\right]iG^{(0)}_{\alpha_1\alpha_2\beta_3\alpha_4}(\omega)\delta_{\alpha_1\beta_1}\delta_{\alpha_2\beta_2}\delta_{\alpha_4\beta_4}\\
&\quad -iG^{(0)}_{\alpha_1\alpha_2\alpha_3\alpha_4}(\omega)\frac{i}{\hbar}\left[\frac{1}{2}\sum_{\rho\delta\lambda}\frac{V_{\alpha_4\lambda,\delta\rho}V_{\delta\rho,\beta_4\lambda}}{\omega-\varepsilon_{\alpha_1}-\varepsilon_{\alpha_2}-\varepsilon_{\alpha_3}-\varepsilon_\rho-\varepsilon_\delta+\varepsilon_\lambda+i\eta}n_\lambda(1-n_\delta)(1-n_\rho)\right]iG^{(0)}_{\alpha_1\alpha_2\alpha_3\beta_4}(\omega)\delta_{\alpha_1\beta_1}\delta_{\alpha_2\beta_2}\delta_{\alpha_3\beta_3},
\end{aligned}
\tag{16}
$$

where,

$$
\omega=\varepsilon_{\alpha_1}+\varepsilon_{\alpha_2}+\varepsilon_{\alpha_3}+\varepsilon_{\alpha_4}. \tag{17}
$$

Here the energy of each nucleon in ^{4}He is a quarter of the energy of the incident ^{4}He, namely,

$$
\varepsilon_{\alpha_1}=\varepsilon_{\alpha_2}=\varepsilon_{\alpha_3}=\varepsilon_{\alpha_4}=\frac{\omega}{4}. \tag{18}
$$

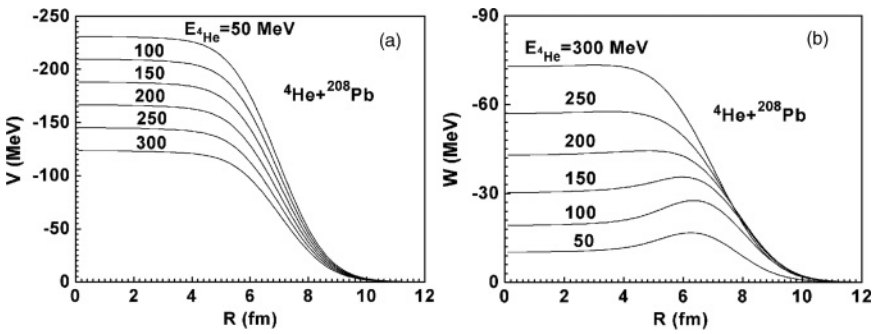

FIG. 4. Radial dependence of ^{4}He MOP for ^{208}Pb. (a) The real parts. (b) The imaginary parts.

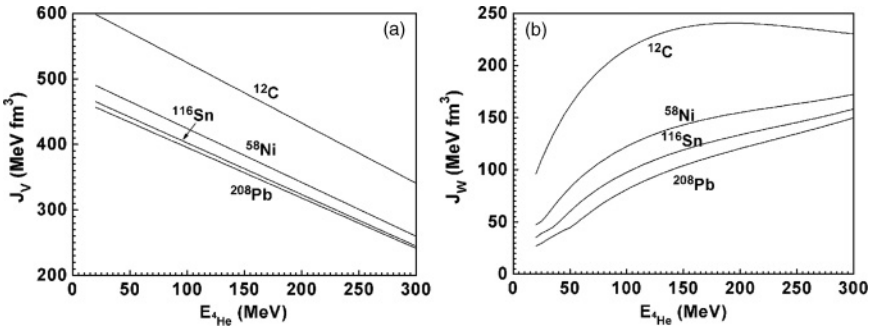

FIG. 5. The volume integral per nucleon of ^{4}He MOP for different nuclei against the incident energy. (a) The real parts. (b) The imaginary parts.

Equation (16) satisfies the second-order term of the the Dyson equation, which is expressed as

$$iG^{(2)}(\alpha_1\alpha_2\alpha_3\alpha_4, \beta_1\beta_2\beta_3\beta_4; \omega) = -\frac{i}{\hbar} iG^{(0)}_{\alpha_1\alpha_2\alpha_3\alpha_4}(\omega) M^{(2)}(\alpha_1\alpha_2\alpha_3\alpha_4, \beta_1\beta_2\beta_3\beta_4; \omega) iG^{(0)}_{\beta_1\beta_2\beta_3\beta_4}(\omega). \tag{19}$$

The second-order mass operator of the four-particle Green's function can be obtained by comparing Eq. (16) with Eq. (19),

$$\begin{aligned} M^{(2)}_{\alpha_1\alpha_2\alpha_3\alpha_4}(E) &= \frac{1}{2}\sum_{\rho\delta\lambda} \frac{V_{\alpha_1\lambda,\delta\rho} V_{\delta\rho,\alpha_1\lambda}}{\varepsilon_{\alpha_1} - \varepsilon_\rho - \varepsilon_\delta + \varepsilon_\lambda + i\eta} n_\lambda(1-n_\delta)(1-n_\rho) + \frac{1}{2}\sum_{\rho\delta\lambda} \frac{V_{\alpha_2\lambda,\delta\rho} V_{\delta\rho,\alpha_2\lambda}}{\varepsilon_{\alpha_2} - \varepsilon_\rho - \varepsilon_\delta + \varepsilon_\lambda + i\eta} n_\lambda(1-n_\delta)(1-n_\rho) \\ &+ \frac{1}{2}\sum_{\rho\delta\lambda} \frac{V_{\alpha_3\lambda,\delta\rho} V_{\delta\rho,\alpha_3\lambda}}{\varepsilon_{\alpha_3} - \varepsilon_\rho - \varepsilon_\delta + \varepsilon_\lambda + i\eta} n_\lambda(1-n_\delta)(1-n_\rho) + \frac{1}{2}\sum_{\rho\delta\lambda} \frac{V_{\alpha_4\lambda,\delta\rho} V_{\delta\rho,\alpha_4\lambda}}{\varepsilon_{\alpha_4} - \varepsilon_\rho - \varepsilon_\delta + \varepsilon_\lambda + i\eta} n_\lambda(1-n_\delta)(1-n_\rho) \\ &= M^{(2)}_{\alpha_1}\left(\frac{E}{4}\right) + M^{(2)}_{\alpha_2}\left(\frac{E}{4}\right) + M^{(2)}_{\alpha_3}\left(\frac{E}{4}\right) + M^{(2)}_{\alpha_4}\left(\frac{E}{4}\right). \end{aligned} \tag{20}$$

The imaginary part of the second-order mass operator $M^{(2)}_{\alpha_1\alpha_2\alpha_3\alpha_4}(E)$ is considered as the imaginary part of the ^{4}He MOP. According to the formula of the principal value integral

$$\frac{1}{x+i\eta} = \mathscr{P}\left(\frac{1}{x}\right) - i\pi\delta(x), \tag{21}$$

the imaginary part of the ^{4}He MOP can be obtained as follows:

$$\begin{aligned} W = \mathrm{Im}M^{(2)}_{\alpha_1\alpha_2\alpha_3\alpha_4}(E) &= -\frac{\pi}{2}\sum_{\rho\delta\lambda} V_{\alpha_1\lambda,\delta\rho} V_{\delta\rho,\alpha_1\lambda} n_\lambda(1-n_\delta)(1-n_\rho)\delta(\varepsilon_{\alpha_1} - \varepsilon_\rho - \varepsilon_\delta + \varepsilon_\lambda) - \frac{\pi}{2}\sum_{\rho\delta\lambda} V_{\alpha_2\lambda,\delta\rho} V_{\delta\rho,\alpha_2\lambda} n_\lambda(1-n_\delta) \\ &\times (1-n_\rho)\delta\left(\varepsilon_{\alpha_2} - \varepsilon_\rho - \varepsilon_\delta + \varepsilon_\lambda\right) - \frac{\pi}{2}\sum_{\rho\delta\lambda} V_{\alpha_3\lambda,\delta\rho} V_{\delta\rho,\alpha_3\lambda} n_\lambda(1-n_\delta)(1-n_\rho)\delta\left(\varepsilon_{\alpha_3} - \varepsilon_\rho - \varepsilon_\delta + \varepsilon_\lambda\right) \\ &-\frac{\pi}{2}\sum_{\rho\delta\lambda} V_{\alpha_4\lambda,\delta\rho} V_{\delta\rho,\alpha_4\lambda} n_\lambda(1-n_\delta)(1-n_\rho)\delta\left(\varepsilon_{\alpha_4} - \varepsilon_\rho - \varepsilon_\delta + \varepsilon_\lambda\right) = \mathrm{Im}M^{(2)}_{\alpha_1}\left(\frac{E}{4}\right) + \mathrm{Im}M^{(2)}_{\alpha_2}\left(\frac{E}{4}\right) \\ &+ \mathrm{Im}M^{(2)}_{\alpha_3}\left(\frac{E}{4}\right) + \mathrm{Im}M^{(2)}_{\alpha_4}\left(\frac{E}{4}\right), \end{aligned} \tag{22}$$

where $\mathrm{Im}M^{(2)}_{\alpha_1}(\frac{E}{4})$, $\mathrm{Im}M^{(2)}_{\alpha_2}(\frac{E}{4})$, $\mathrm{Im}M^{(2)}_{\alpha_3}(\frac{E}{4})$, and $\mathrm{Im}M^{(2)}_{\alpha_4}(\frac{E}{4})$ are the contributions of the imaginary parts of the MOP for the nucleons [10] in ^{4}He respectively. An important conclusion is obtained from Eqs. (15) and (22) that, as the indirect interaction of the nucleons in ^{4}He is ignored, the ^{4}He MOP is the sum of the microscopic optical potentials for its constituent nucleons. The interaction V in Eq. (12) is given by the extended Skyrme force GS2 as in Refs. [10–12]. This force can describe successfully some ground-state properties, such as effective mass, single-particle energy, and so on [18]; moreover, it is the best one to be applied to fit the experimental data of nuclear reaction, which is shown in the next section.

In the nuclear matter, the nucleon wave function in Eq. (12) is given by the plane wave

$$\varphi_\alpha(\vec{r}) = \frac{1}{\sqrt{\Omega}} e^{i\vec{k_\alpha}\cdot\vec{r}}\chi_{\sigma_\alpha}\chi_{\tau_\alpha}, \tag{23}$$

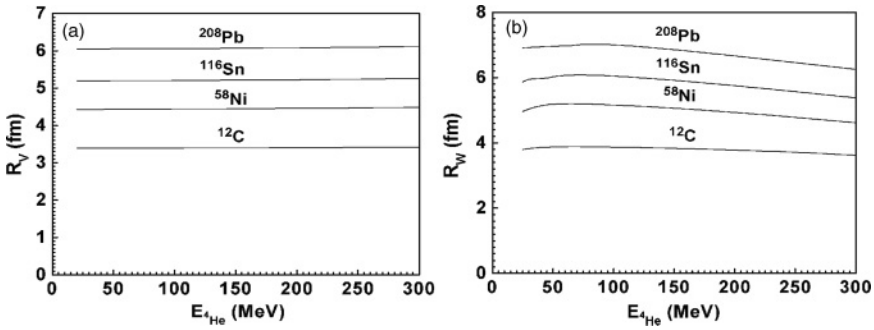

FIG. 6. The root mean square radii of ^{4}He MOP for different nuclei against incident energy. (a) The real parts. (b) The imaginary parts.

where χ_{σ_α} and χ_{τ_α} are the spin and isospin wave functions, respectively, and Ω is the volume.

When the distribution of the nucleons in ^{4}He is considered, the ^{4}He MOP can be obtained by folding the microscopic optical potentials of its constituent nucleons in the ground state of ^{4}He. In the relative coordinate representation, the ^{4}He MOP can be expressed as

$$\begin{aligned} V_{^4\mathrm{He}}(R) = \langle \phi_{^4\mathrm{He}} | & V_n\left(\vec{R} + \tfrac{1}{2}\vec{\xi_1} + \tfrac{1}{2}\vec{\xi_3}\right) \\ & + V_n\left(\vec{R} - \tfrac{1}{2}\vec{\xi_1} + \tfrac{1}{2}\vec{\xi_3}\right) \\ & + V_p\left(\vec{R} + \tfrac{1}{2}\vec{\xi_2} - \tfrac{1}{2}\vec{\xi_3}\right) \\ & + V_p\left(\vec{R} - \tfrac{1}{2}\vec{\xi_2} - \tfrac{1}{2}\vec{\xi_3}\right) | \phi_{^4\mathrm{He}} \rangle, \end{aligned} \tag{24}$$

where

$$\begin{cases} \vec{R} = \frac{1}{4}(\vec{r_1} + \vec{r_2} + \vec{r_3} + \vec{r_4}), \\ \vec{\xi_1} = \vec{r_1} - \vec{r_2}, \\ \vec{\xi_2} = \vec{r_3} - \vec{r_4}, \\ \vec{\xi_3} = \frac{1}{2}[(\vec{r_1} + \vec{r_2}) - (\vec{r_3} + \vec{r_4})], \end{cases} \tag{25}$$

with $\vec{R}$ indicating the position of the center of mass of the ^{4}He and $\vec{r_1}$, $\vec{r_2}$, $\vec{r_3}$, and $\vec{r_4}$ indicating the position of the nucleons in ^{4}He. V_n and V_p are the microscopic optical potentials for the neutrons and the protons in ^{4}He, respectively, with a quarter of the incident ^{4}He energy. The expressions of V_n and V_p are taken as those in Ref. [10]. $\phi_{^4\mathrm{He}}$ is the ground-state wave function of ^{4}He, which can be expressed as

$$\phi_{^4\mathrm{He}} = \left(\frac{\beta^3}{4\pi^3}\right)^{\frac{3}{4}} e^{-\frac{\beta}{4}(\xi_1^2+\xi_2^2)-\frac{\beta}{2}\xi_3^2}, \tag{26}$$

where $\beta = 0.4395$.

The local density approximation [19,20] is also used to obtain the MOP for finite nuclei as in Refs. [10–12].

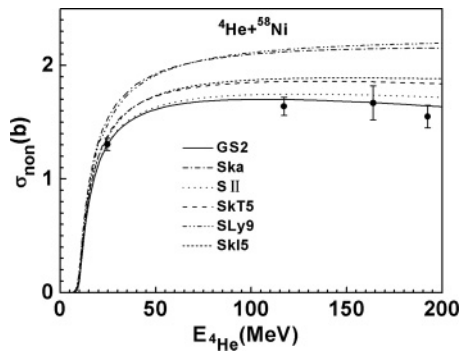

FIG. 7. Comparison of the calculated reaction cross sections for ^{4}He + ^{58}Ni reaction using GS2 (solid line), Ska (dash-dotted line), SII (dotted line), SkT5 (dashed line), SLy9 (dash-dot-dotted line), and SkI5 (short-dashed line) with experimental data (symbols) [28,29].

III. CALCULATED RESULTS AND ANALYSIS

The ^{4}He MOP obtained is analyzed and used to predict the reaction cross sections and elastic scattering angular distributions for different target nuclei from ^{12}C to ^{209}Bi.

The radial dependence of the real and imaginary parts of the ^{4}He MOP for ^{58}Ni and ^{208}Pb at incident energies of 50, 100, 150, 200, 250, and 300 MeV is shown in Figs. 3 and 4. In Figs. 3(a) and 4(a), the absolute value of the real part decreases with increasing radius and incident energy. In Figs. 3(b) and 4(b), the absolute value of the imaginary part increases with increasing energy of incident ^{4}He, and the dominant contribution of the imaginary part changes from the surface absorption to the volume absorption as the incident energy increases.

The volume integrals per nucleon of the real and imaginary parts of the ^{4}He MOP for ^{12}C, ^{58}Ni, ^{116}Sn, and ^{208}Pb are shown in Fig. 5, which decrease with increasing mass number. The volume integral per nucleon of the real part is linearly dependent on the incident energy and decreases as the energy of the incident ^{4}He increases, while the volume integral per nucleon of the imaginary part increases with increasing energy.

The root mean square radii of the real and imaginary parts of the MOPs for ^{12}C, ^{58}Ni, ^{116}Sn, and ^{208}Pb are also given in Fig. 6. It is shown the root mean square radii of the MOPs increase with increasing mass number, and keep basically as a constant for each target nucleus.

The ^{4}He reaction cross sections for ^{12}C, ^{16}O, ^{28}Si, ^{40}Ca, ^{58,60}Ni, ^{112,116,120,124}Sn, ^{208}Pb, and ^{209}Bi are calculated using different Skyrme forces including GS2, SkP [21], Ska [22], SII [23], SkT1-SkT9 [24], SLy0-SLy10 [25,26], and SkI1-SkI5 [27]. The comparisons between the calculated results and the experimental data [28–33] show that the calculated

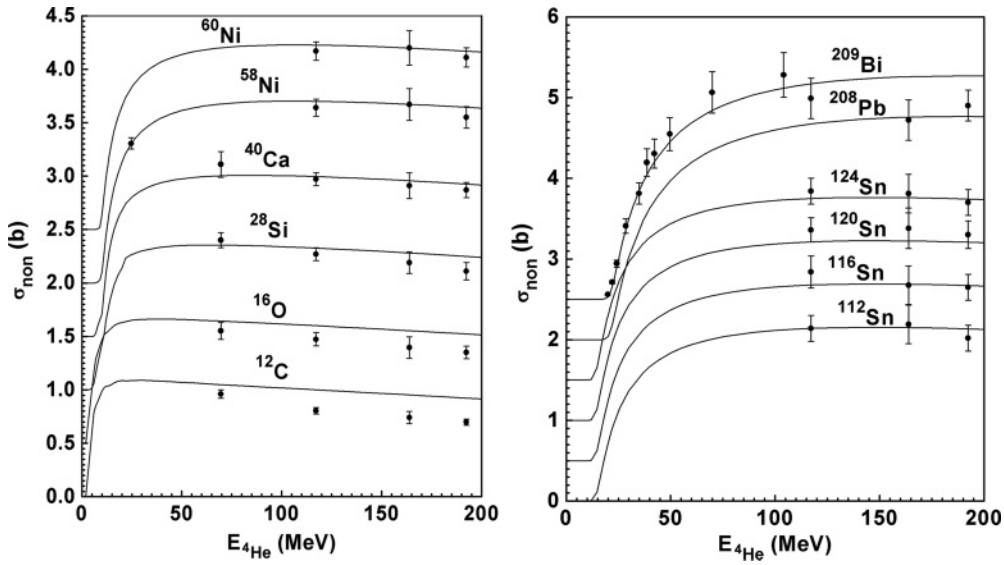

FIG. 8. Comparison between the calculated reaction cross sections (solid line) and experimental data (symbols) [28–33] for ^{4}He + ^{12}C, ^{16}O, ^{28}Si, ^{40}Ca, ^{58,60}Ni, ^{112,116,120,124}Sn, ^{208}Pb, and ^{209}Bi reactions. Different data sets are added by 0, 0.5, 1, 1.5, 2, and 2.5.

result by GS2 is the best in fitting the experimental data. The comparisons of the calculated results of ^{4}He reaction cross sections for ^{58}Ni using GS2, Ska, S, SkT5, SLy9, and SkI5 with the experimental data are given in Fig. 7 as an example. It is shown that the calculated result by GS2 fits the experimental data best. Therefore, GS2 is adopted to calculate the microscopic optical potential for ^{4}He in this paper.

The comparisons between calculated results of the ^{4}He reaction cross sections and the experimental data for ^{12}C, ^{16}O, ^{28}Si, ^{40}Ca, ^{58,60}Ni, ^{112,116,120,124}Sn, ^{208}Pb, and ^{209}Bi are given in Fig. 8. The figure shows that the calculated results for ^{28}Si, ^{40}Ca, ^{58,60}Ni, ^{112,116,120,124}Sn, ^{208}Pb, and ^{209}Bi are in good agreement with the experimental data. The shapes of the calculated curves of reaction cross sections for ^{12}C and ^{16}O are similar to those of the experimental data, but the magnitudes of the calculated results and the experimental data have discrepancy. Figure 8 also shows there is a general trend that the reaction cross sections increase with increasing mass number of the target nuclei and that the reaction cross sections for heavy nuclei increase with increasing incident energy from threshold up to 200 MeV, while for light nuclei the reaction

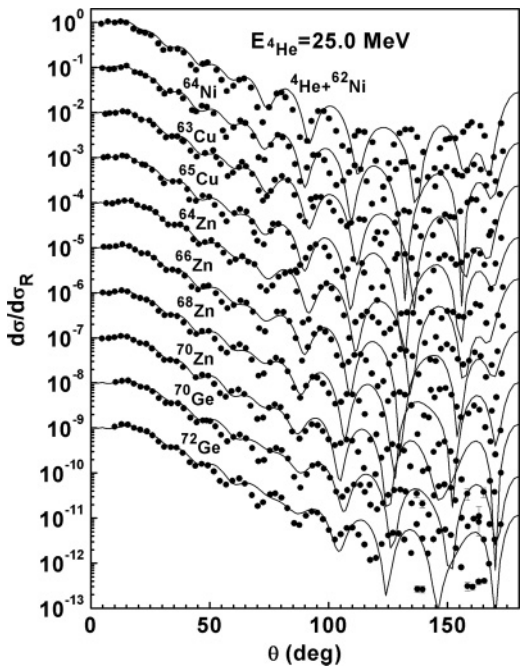

FIG. 9. Calculated elastic scattering angular distributions in the Rutherford ratio (solid line) at incident ^{4}He energy of 25.0 MeV compared with experimental data (symbols) [34]. The results are divided by 10^{0}, 10^{1}, 10^{2}, ….

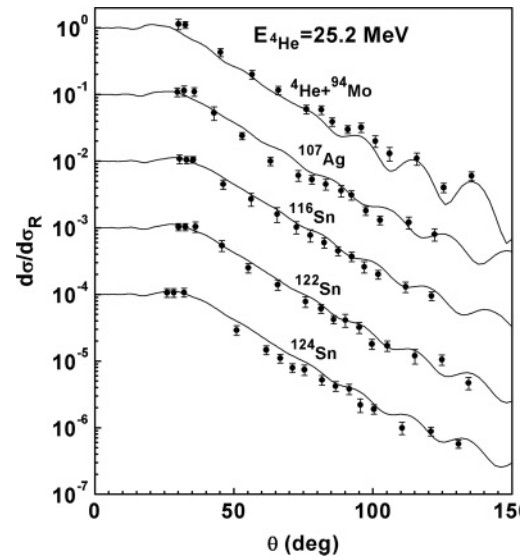

FIG. 10. Calculated elastic scattering angular distributions in the Rutherford ratio (solid line) at incident ^{4}He energy of 25.2 MeV compared with experimental data (symbols) [35]. The results are divided by 10^{0}, 10^{1}, 10^{2}, ….

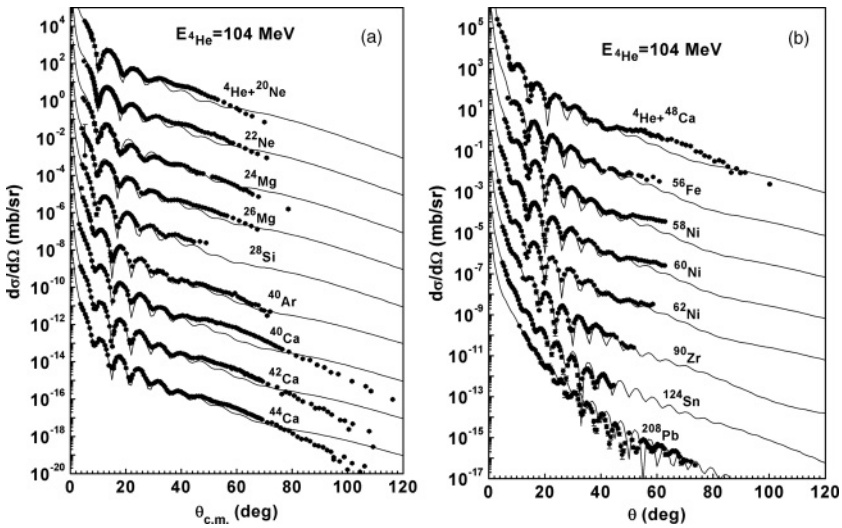

FIG. 11. Calculated elastic scattering angular distributions (solid line) at incident ^{4}He energy of 104 MeV compared with experimental data (symbols) [32,36,37]. The results are divided by 10^0, 10^1, 10^2, ...

cross sections increase first and then decrease with increasing incident energy.

The calculated results of the differential cross sections relative to Rutherford cross sections for ^{62,64}Ni, ^{63,65}Cu, ^{64,66,68,70}Zn, and ^{70,72}Ge at incident ^{4}He energy of 25.0 MeV are compared with the experimental data [34] in Fig. 9. The theoretical results are in reasonable agreement with the experimental data. The calculated results of elastic scattering angular distributions of ^{4}He for ^{94}Mo, ^{107}Ag, and ^{116,122,124}Sn at incident energy of 25.2 MeV are also compared with the experimental data [35] in Fig. 10, and good agreement can be observed.

The comparisons of the calculated results of elastic scattering angular distributions for different target nuclei from ^{20}Ne to ^{208}Pb with experimental data [32,36,37] at incident ^{4}He energy of 104.0 MeV are given in Fig. 11. For the targets from ^{20}Ne to ^{60}Ni, a good agreement is obtained for the angle below 50°, while for the larger angle, there are a few discrepancies between the magnitudes of calculated results and the experimental data. For the other targets, the calculated results are in good agreement with experimental data.

The calculated results of the elastic scattering angular distributions for ^{16}O, ^{46,48}Ti, ^{58}Ni, ^{116}Sn, and ^{197}Au at incident ^{4}He energy of 240.0 MeV are compared with the experimental data [38–41] in Fig. 12. Except for ^{46}Ti at larger angles, The theoretical values are in good agreement with the experimental data for all the targets.

The elastic scattering angular distributions for different targets from ^{12}C to ^{208}Pb at incident ^{4}He energy 386.0 MeV were measured [42]. The comparisons of present calculated

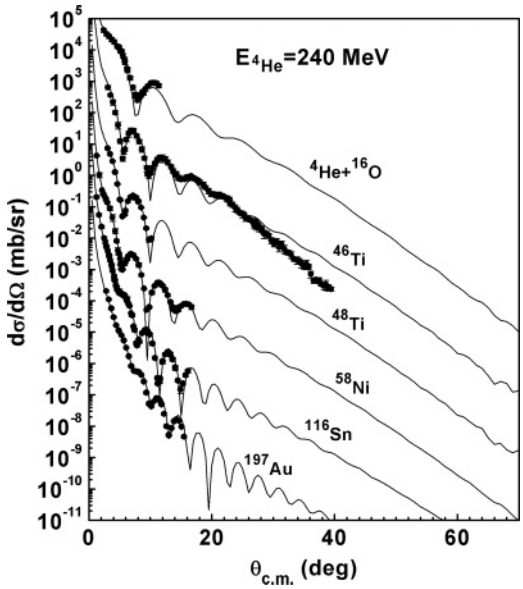

FIG. 12. Calculated elastic scattering angular distributions (solid line) at incident ^{4}He energy of 240 MeV compared with experimental data (symbols) [38–41]. The results are divided by 10^0, 10^1, 10^2, ...

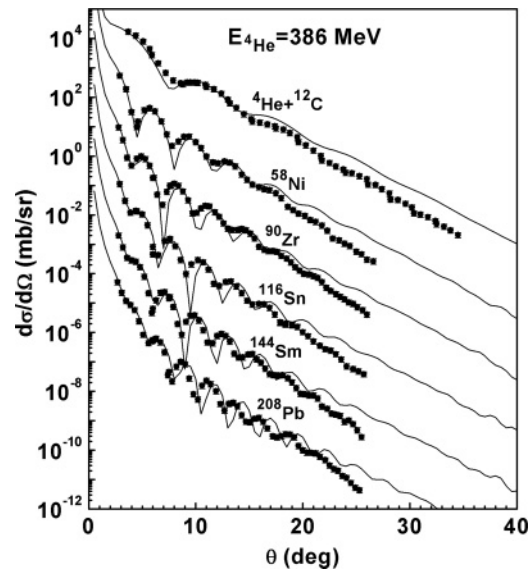

FIG. 13. Calculated elastic scattering angular distributions (solid line) at incident ^{4}He energy of 386.0 MeV compared with experimental data (symbols) [42]. The results are divided by 10^0, 10^1, 10^2, ...

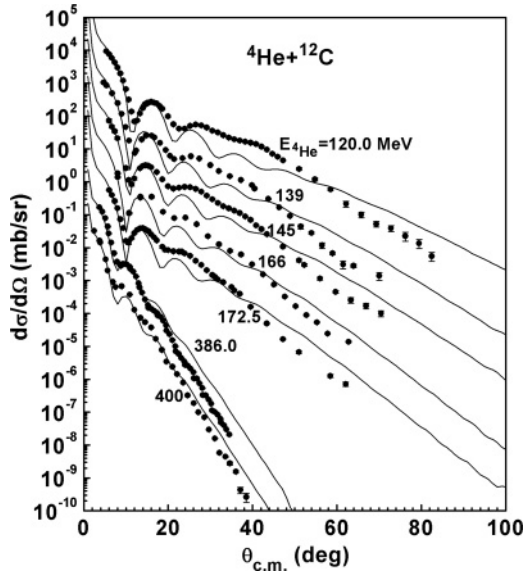

FIG. 14. Calculated elastic scattering angular distributions (solid line) at different incident ^{4}He energies compared with experimental data (symbols) [43–46] for ^{4}He + ^{12}C reaction. The results are divided by 10^0, 10^1, 10^2, ...

results with the experimental data in Fig. 13 show that a reasonable agreement is obtained.

The calculated results of differential cross sections relative to Rutherford cross sections for elastic scattering of ^{4}He from ^{12}C at incident energies from 120 to 400 MeV are compared with the experimental data [43–46] in Fig. 14. The calculated results are in reasonable agreement with the experimental data.

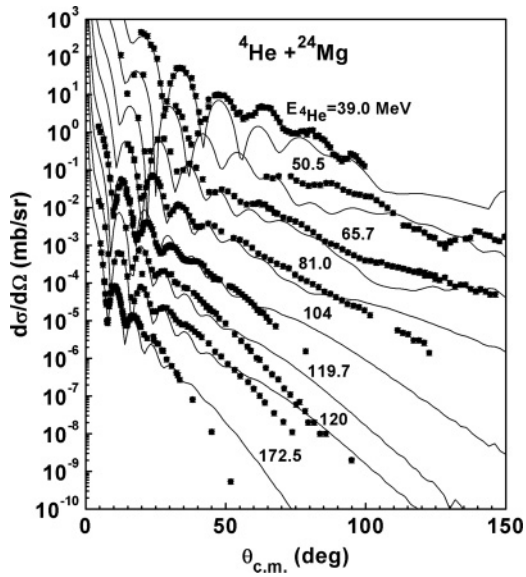

FIG. 15. Calculated elastic scattering angular distributions (solid line) at different incident ^{4}He energies compared with experimental data (symbols) [36,43,47,48] for ^{4}He + ^{24}Mg reaction. The results are divided by 10^0, 10^1, 10^2, ...

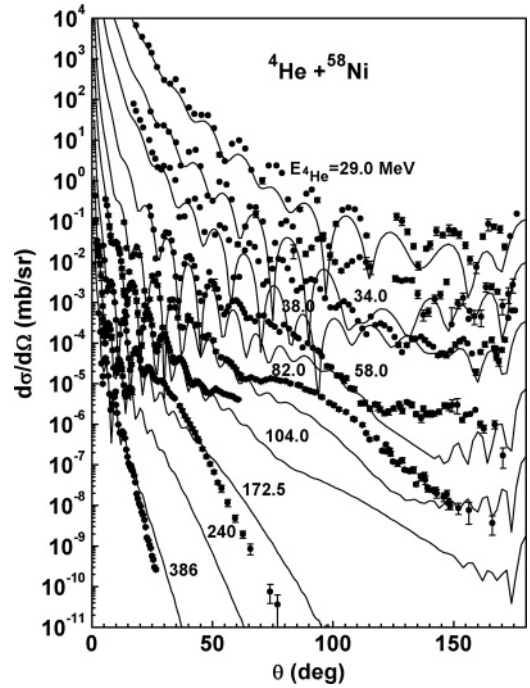

FIG. 16. Calculated elastic scattering angular distributions (solid line) at different incident ^{4}He energies compared with experimental data (symbols) [37,40,42,49–51] for ^{4}He + ^{58}Ni reaction. The results are divided by 10^0, 10^1, 10^2, ...

The comparison between the calculated elastic scattering angular distributions and experimental data [36,43,47,48] for ^{24}Mg at incident ^{4}He energies from 39.0 to 172.5 MeV is given in Fig. 15. It is shown that for the angle less than 50°, the calculated results are in good agreement with the experimental data, while for the larger angle, there are a few

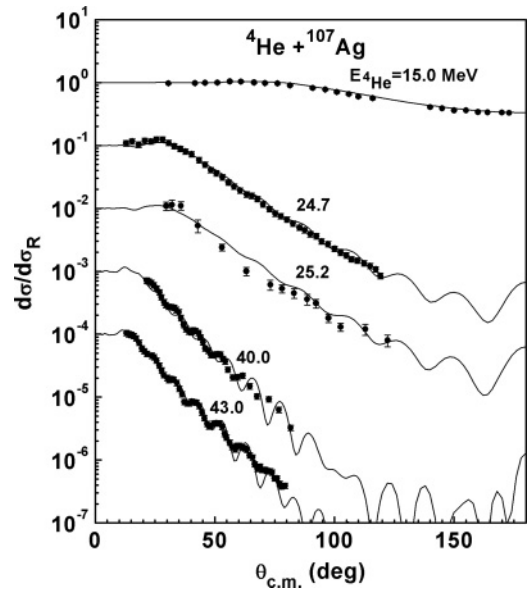

FIG. 17. Calculated elastic scattering angular distributions in the Rutherford ratio (solid line) at different incident ^{4}He energies compared with experimental data (symbols) [35,52–55] for ^{4}He + ^{107}Ag reaction. The results are divided by 10^0, 10^1, 10^2, ...

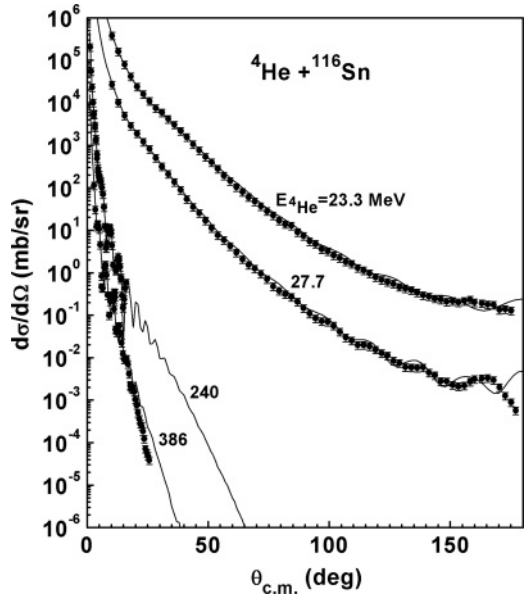

FIG. 18. Calculated elastic scattering angular distributions (solid line) at different incident ^{4}He energies compared with experimental data (symbols) [40,42,56] for ^{4}He + ^{116}Sn reaction. The results are divided by 10^0, 10^1, 10^2, ….

discrepancies between the magnitudes of calculated results and the experimental data.

The calculated results of elastic scattering angular distributions for ^{58}Ni at incident ^{4}He energies from 29.0 to 386.0 MeV are compared with the experimental data [37,40,42,49–51] in Fig. 16. The calculated results are in reasonable agreement with the experimental data.

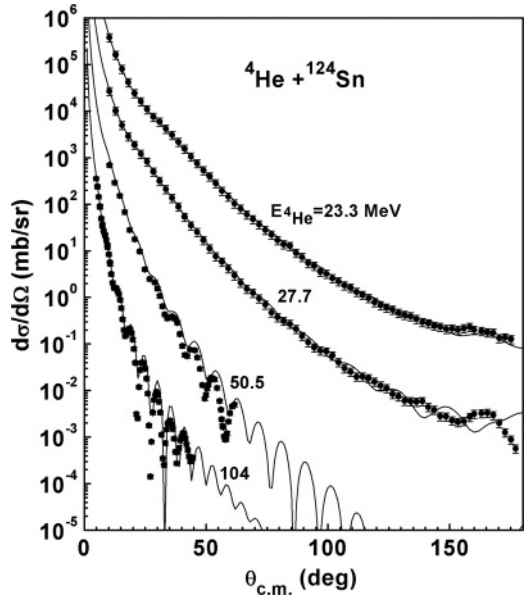

FIG. 19. Calculated elastic scattering angular distributions (solid line) at different incident ^{4}He energies compared with experimental data (symbols) [32,56] for ^{4}He + ^{124}Sn reaction. The results are divided by 10^0, 10^1, 10^2, ….

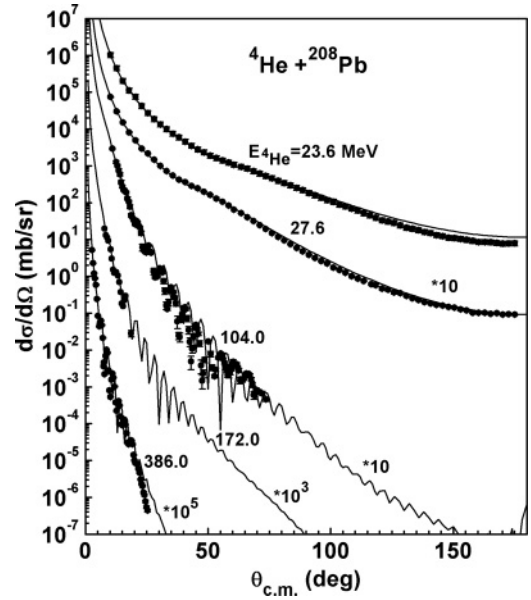

FIG. 20. Calculated elastic scattering angular distributions (solid line) at different incident ^{4}He energies compared with experimental data (symbols) [32,42,56,57] for ^{4}He + ^{208}Pb reaction.

The calculated results of differential cross sections relative to Rutherford cross sections for ^{107}Ag at incident ^{4}He energies from 15.0 to 43.0 MeV are compared with the experimental data [35,52–55] in Fig. 17. It shows a good agreement.

The elastic scattering angular distributions for natural target Sn at incident ^{4}He energies of 23.3 and 27.7 MeV [56] and for

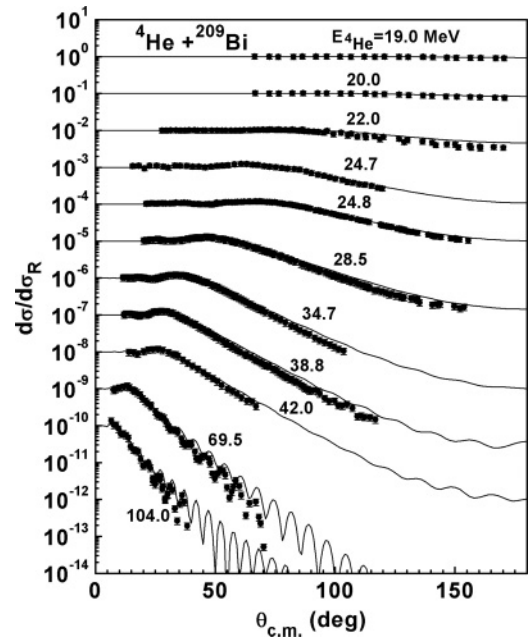

FIG. 21. Calculated elastic scattering angular distributions in the Rutherford ratio (solid line) at different incident ^{4}He energies compared with experimental data (symbols) [30,33,53] for ^{4}He + ^{209}Bi reaction. The results are divided by 10^0, 10^1, 10^2, ….

the corresponding isotope targets ^{116}Sn at incident energies of 240.0 and 386.0 MeV [40,42] and ^{124}Sn at incident energies of 50.5 and 104.0 MeV [32] were measured respectively. The calculated elastic scattering angular distributions for isotope targets ^{116}Sn and ^{124}Sn at different energies are compared with these experimental data in Fig. 18 and 19. It is shown that the calculated results are in good agreement with the experimental data except for the data for natural target Sn at the angles larger than 160°.

The comparisons between the calculated results of elastic scattering angular distributions and experimental data [32,42,56,57] for ^{208}Pb at incident ^{4}He energies from 23.6 to 386.0 MeV are shown in Fig. 20. The calculated results are in good agreement with the experimental data.

Figure 21 shows the comparison of the calculated results of differential cross sections relative to Rutherford cross sections for ^{209}Bi at incident ^{4}He energies from 19 to 104 MeV with the experimental data [30,33,53]. The calculated results are in good agreement with experimental data.

It can be found that there is a bit of discrepancy between the calculated results and experimental data of the reaction cross sections for ^{12}C and ^{16}O and some elastic scattering angular distributions for light nuclei at larger angles. The reasons for that are as follows: First of all, the light nuclei show strong nuclear structure effect; also, the recoil effect is obvious for light nuclei; in addition, the traditional Skyrme interactions are developed by fitting the ground-state nuclear properties, maybe they need to be adjusted to adapt to the case of nuclear reaction.

IV. SUMMARY

The ^{4}He MOP is obtained by Green's function method. The real part and the imaginary part of the ^{4}He MOP are obtained by the first-order mass operator and the imaginary part of second-order mass operator of the four-particle Green's function, respectively. The radial dependence, the volume integral per nucleon and the root mean square radii of the MOP are calculated, and the trend of the results is reasonable. The reaction cross sections and elastic scattering angular distributions for target nuclides in the mass range $12 \leqslant A \leqslant 209$ with incident energies up to 400 MeV are also calculated by the MOP, and compared with the experimental data. The calculated results are in good agreement with the experimental data generally.

There is a bit of discrepancy between a few of the calculated results and the experimental data. This may suggest that a new set of Skyrme interactions, which cannot only describe the ground-state nuclear properties, but also well reproduce the nuclear reaction data, need to be developed to improve the model calculation. This will be studied in the future.

ACKNOWLEDGMENTS

This work is one of National Basic Research Program of China (973 Program), which is Key Technology Research of Accelerator Driven Sub-critical System for Nuclear Waste Transmutation, and supported by the China Ministry of Science and Technology under Contract No. 2007CB209903.

[1] G. R. Satchler and W. G. Love, Phys. Rep. **55**, 183 (1979).
[2] W. G. Love, Phys. Rev. C **17**, 1876 (1978).
[3] P. Mohr *et al.*, Phys. Rev. C **55**, 1523 (1997).
[4] D. T. Khoa, Phys. Rev. C **63**, 034007 (2001).
[5] G. Bertsch *et al.*, Nucl. Phys. A **284**, 399 (1977).
[6] D. T. Khoa, G. R. Satchler, and W. von Oertzen, Phys. Rev. C **56**, 954 (1997).
[7] V. Lapoux *et al.*, Phys. Rev. C **66**, 034608 (2002).
[8] T. Furumoto and Y. Sakuragi, Phys. Rev. C **74**, 034606 (2006).
[9] W. Zou, Y. Tian, and Z. Y. Ma, Phys. Rev. C **78**, 064613 (2008).
[10] Q. B. Shen, Y. L. Han, and H. R. Guo, Phys. Rev. C **80**, 024604 (2009).
[11] H. Guo, Y. Xu, Y. Han, and Q. Shen, Phys. Rev. C **81**, 044617 (2010).
[12] H. Guo, Y. Zhang, Y. Han, and Q. Shen, Phys. Rev. C **79**, 064601 (2009).
[13] J. S. Bell and E. J. Squires, Phys. Rev. Lett. **3**, 96 (1959).
[14] C. Mahaux and R. Sartor, Phys. Rev. C **19**, 229 (1979).
[15] S. S. Wu and T. T. S. Kuo, Nucl. Phys. A **430**, 110 (1984).
[16] P. Schuck, Z. Phys. **241**, 395 (1971).
[17] J. Dukelsky, G. Ropke, and P. Schuck, Nucl. Phys. A **628**, 17 (1998).
[18] S. Krewald, V. Klemt, J. Speth, and A. Faessler, Nucl. Phys. A **281**, 166 (1977).
[19] J. W. Negele, Phys. Rev. C **1**, 1260 (1970).
[20] J. P. Jeukenne, A. Lejeune, and C. Mahaux, Phys. Rev. C **16**, 80 (1977).
[21] J. Dobaczewski, H. Flocard, and J. Treiner, Nucl. Phys. A **422**, 103 (1984).
[22] H. S. Kohler, Nucl. Phys. A **258**, 301 (1976).
[23] D. Vautherin and D. M. Brink, Phys. Rev. C **5**, 626 (1972).
[24] F. Tondeur, M. Brack, M. Farine, and J. M. Pearson, Nucl. Phys. A **420**, 297 (1984).
[25] E. Chabanat *et al.*, Nucl. Phys. A **627**, 710 (1997).
[26] E. Chabanat *et al.*, Nucl. Phys. A **635**, 231 (1998).
[27] P. Reinhard and H. Flocard, Nucl. Phys. A **584**, 467 (1995).
[28] A. Ingemarsson *et al.*, Nucl. Phys. A **676**, 3 (2000).
[29] A. Budzanowski *et al.*, Nucl. Phys. A **106**, 21 (1967).
[30] A. R. Barnett and J. S. Lilley, Phys. Rev. C **9**, 2010 (1974).
[31] J. Alster, Phys. Rev. **141**, 1138 (1966).
[32] G. Hauser *et al.*, Nucl. Phys. A **128**, 81 (1969).
[33] P. Singh, A. Chatterjee, S. K. Gupta, and S. S. Kerekatte, Phys. Rev. C **43**, 1867 (1991).
[34] F. Ballester *et al.*, J. Phys. G **13**, 1541 (1987).
[35] O. V. Bespalova *et al.*, Izv. Ross. Akad. Nauk, Ser. Fiz. **56**, 113 (1992).
[36] H. Rebel *et al.*, Nucl. Phys. A **182**, 145 (1972).
[37] H. Rebel, R. Lohken, G. W. Schweimer, G. Schatz, and G. Hauser, Z. Phys. **256**, 258 (1972).
[38] Y. W. Lui, H. L. Clark, and D. H. Youngblood, Phys. Rev. C **64**, 064308 (2001).

[39] Y. Tokimoto, Y. W. Lui, H. L. Clark, B. John, X. Chen, and D. H. Youngblood, Phys. Rev. C **74**, 044308 (2006).
[40] H. L. Clark, Y. W. Luib, and D. H. Youngblood, Nucl. Phys. A **589**, 416 (1995).
[41] H. L. Clark, D. H. Youngblood, and Y. W. Lui, Phys. Rev. C **54**, 72 (1996).
[42] M. Uchida *et al.*, Phys. Rev. C **69**, 051301 (2004).
[43] S. Wiktor *et al.*, Acta Phys. Pol. B **12**, 491 (1981).
[44] I. Brissaud, M. K. Brussel, M. Sowinski, and B. Tatischeff, Phys. Lett. B **30**, 324 (1969).
[45] T. Wakasa *et al.*, Phys. Lett. B **653**, 173 (2007).
[46] S. M. Smith *et al.*, Nucl. Phys. A **207**, 273 (1973).
[47] S. Ya. Aisina, K. A. Kuterbekov, N. N. Pavlova, and A. V. Yushkov, Izv. Ross. Akad. Nauk, Ser. Fiz. **53**, 37 (1989).
[48] M. Pignanelli, S. Micheletti, R. De Leo, S. Brandenburg, and M. N. Harakeh, Phys. Rev. C **33**, 40 (1986).
[49] J. Albinski *et al.*, Nucl. Phys. A **445**, 477 (1985).
[50] A. Budzanowski *et al.*, Phys. Rev. C **17**, 951 (1978).
[51] H. H. Chang *et al.*, Nucl. Phys. A **270**, 413 (1976).
[52] B. D. Watson, D. Robson, D. D. Tolbert, and R. H. Davis, Phys. Rev. C **4**, 2240 (1971).
[53] A. Budzanowski *et al.*, Phys. Lett. **11**, 74 (1964).
[54] G. Igo, H. E. Wegner, and R. M. Eisberg, Phys. Rev. **101**, 1508 (1956).
[55] J. L. Yntema, B. Zeidman, and B. J. Raz, Phys. Rev. **117**, 801 (1960).
[56] W. Karcz, I. Kluska, Z. Sanok, J. Szmider, J. Szymakowski, S. Wiktor, and R. Wolski, Acta Phys. Pol. B **3**, 525 (1972).
[57] H. P. Morsch, C. Sukosd, M. Rogge, P. Turek, H. Machner, and C. Mayer-Boricke, Phys. Rev. C **22**, 489 (1980).